PAPER • OPEN ACCESS

Seeds of phase transition to thermoacoustic instability

To cite this article: M Raghunathan *et al* 2022 *New J. Phys.* **24** 063008

View the article online for updates and enhancements.

New Journal of Physics

The open access journal at the forefront of physics

CrossMark

PAPER

Seeds of phase transition to thermoacoustic instability

M Raghunathan[1], N B George[2,3,*] [ID], V R Unni[4], R I Sujith[1], J Kurths[2,3] and E Surovyatkina[2,5]

1 Department of Aerospace Engineering, Indian Institute of Technology, Madras, India
2 Potsdam Institute for Climate Impact Research, Potsdam, Germany
3 Department of Physics, Humboldt University of Berlin, Berlin, Germany
4 Department of Mechanical and Aerospace Engineering, Indian Institute of Technology, Hyderabad, India
5 Space Research Institute of Russian Academy of Sciences, Moscow, Russia
* Author to whom any correspondence should be addressed.

E-mail: george@pik-potsdam.de

Abstract

Tackling the problem of emissions is at the forefront of scientific research today. While industrial engines designed to operate in stable regimes produce emissions, attempts to operate them at 'greener' conditions often fail due to a dangerous phenomenon known as thermoacoustic instability. Hazardous high amplitude periodic oscillations during thermoacoustic instability lead to the failure of these engines in power plants, aircraft, and rockets. To prevent this catastrophe in the first place, identifying the onset of thermoacoustic instability is required. However, detecting the onset is a major obstacle preventing further progress due to spatiotemporal variability in the reacting field. Here, we show how to overcome this obstacle by discovering a critical condition in certain zones of the combustor, which indicates the onset of thermoacoustic instability. In particular, we reveal the critical value of the local heat release rate that allows us to distinguish stable operating regimes from hazardous operations. We refer to these zones as seeds of the phase transition because they show the earliest manifestation of the impending instability. The increase in correlations in the heat release rate between these zones indicates the transition from a chaotic state to a periodic state. Remarkably, we found that observations at the seeds of the phase transition enable us to predict when the onset occurs, well before the emergence of dangerous large-amplitude periodic acoustic pressure oscillations. Our results contribute to the operation of combustors in more environment-friendly conditions. The presented approach is applicable to other systems exhibiting such phase transitions.

1. Introduction

All combustion engines in automobiles, airplanes, ships etc produce emissions. But industrial systems produce more emissions such as oxides of nitrogen and sulphur due to high flame temperatures. To reduce these emissions and operate in 'greener' conditions, we need to lower the flame temperatures. Increasing the proportion of air to the fuel reduces the flame temperature. However, such 'greener' operations often result in the dangerous phenomenon of thermoacoustic instability, which results in large amplitude oscillations leading to catastrophic consequences. Controlling the occurrence of thermoacoustic instability creates opportunities to operate under 'greener' conditions. But the major problem is in identifying the onset of thermoacoustic instability. This is a problem that has been documented in various systems, but still remains a challenging one (Biggs 2009, Blomshield *et al* 1997, Sutton 2003, Lieuwen and Yang 2005, McManus *et al* 1993, Lieuwen 2002, Ducruix *et al* 2003, Juniper and Sujith 2018). Thermoacoustic instability occurs because of the coupling between the flame and the acoustics field within the combustion chamber(McManus *et al* 1993, Akkerman and Law 2013, Moon *et al* 2020) reinforced by emerging large coherent structures or vortices in the flow field (Poinsot *et al* 1987, Schadow *et al* 1989).

Turbulent flow systems are characterized by chaotic or disordered behaviour. However, at certain conditions they have organized flow structures (Kline *et al* 1967, Brown and Roshko 1974, Cantwell 1981). The emergence of such ordered spatiotemporal patterns is ubiquitous in ecology (Ball and Borley 1999, Meron 2016), climate (Rastogi *et al* 2016, Chang *et al* 2016), chemistry (Busse 1978, Croquette 1989), biology (Ball and Borley 1999, Kanders *et al* 2020), engineering (Cross and Hohenberg 1993, Bayliss and Matkowsky 1991), etc. Such regularities in the spatiotemporal behaviour appear near a phase transition, when certain system parameters move beyond a critical point (Scheffer *et al* 2001, Yang *et al* 2012, Kanders *et al* 2020). This phase transition demarcates two contrasting regimes of the system. However, identifying the impending phase transition is quite often a challenge, since there is no visible change in the dynamics as the system approaches the critical point.

Recently, progress has been made towards the solution of identifying the phase transition, wherein some studies on spatiotemporal systems show that while a phase transition occurs for the whole system, there may be regions where such transitions emerge earlier. In a study on the Indian monsoon prediction, Stolbova *et al* (2016) uncovered two unique locations in the Indian subcontinent (referred to as tipping elements), where critical conditions originate and then propagate in a certain direction that results in the transition from pre-monsoon to monsoon; the regularities between the tipping elements allows a long term prediction of the monsoon onset. In short, it is necessary to locate such zones to identify the origin of the phase transition. In this paper, we focus on the identification of such zones in a turbulent combustion system. We utilize the phenomenon of critical growth of fluctuations (Surovyatkina 2004, Surovyatkina *et al* 2005) as an indicator of the onset of such a phase transition.

In particular, we investigate the spatiotemporal dynamics in a confined reactive turbulent system when it approaches the state of thermoacoustic instability (S_{TI}). In this system, flow perturbations cause heat release rate fluctuations from the flame, which subsequently generates sound waves. Next, these sound waves get reflected from the boundaries back to the source and further modify the heat release rate fluctuations. This process results in a positive feedback, when the acoustic pressure fluctuations due to the sound waves and the unsteady heat release rate become in phase (Rayleigh 1878). Such a positive feedback favours the growth of acoustic oscillations, leading to periodic temporal dynamics (McManus *et al* 1993, Lieuwen 2002, Ducruix *et al* 2003, Juniper and Sujith 2018) and the periodic emergence of spatially organized patterns (Candel 1992, Lieuwen 2012, Sujith and Unni 2020a, 2020b). Notably, the dangerous high amplitude periodic oscillations of acoustic pressure during S_{TI} cause significant losses to the power and propulsion industry by causing structural failure, damaging the navigation and control system, overwhelming the thermal protection system, etc (Lieuwen 2002, 2012, Juniper and Sujith 2018). The onset of periodic oscillations (S_{TI}) occurs via a transition from a state of chaotic fluctuations (S_C), through the state of intermittency (S_{IN}) (Gotoda *et al* 2011, Nair *et al* 2014, Delage *et al* 2017).

Different spatiotemporal patterns characterize each state of the system. It was recently discovered that S_C, referred to as combustion noise, is chaotic (Nair *et al* 2013, Tony *et al* 2015). S_C is also characterized by disorganized flow and flame dynamics (Mondal *et al* 2017, George *et al* 2018, Raghunathan *et al* 2020). During S_{IN}, bursts of periodic oscillations appear amidst epochs of aperiodic dynamics at apparently random intervals (Nair *et al* 2014). Additionally, during S_{IN}, macroscopic patterns at the size of the system geometry emerge during the regime of periodic oscillations, while disordered small-scale structures exist during the regime of aperiodic oscillations (Mondal *et al* 2017, George *et al* 2018, Raghunathan *et al* 2020). On the other hand, S_{TI} typically exhibits the coexistence of large-scale coherent flow structures or vortices, spatially and temporally organized reaction fields, distinct standing wave modes, large-amplitude periodic acoustic pressure oscillations etc (George *et al* 2018). In fact, during the transition from S_C to S_{TI} via S_{IN}, the disordered dynamics decreases continuously, while the ordered dynamics increases through the collective behaviour of small-scale structures (George *et al* 2018, Raghunathan *et al* 2020). This continuous evolution makes it difficult to identify the critical point of the system parameter or the onset of S_{TI}, which is crucial for designing safe operating regimes of such complex spatiotemporal systems. Further, whether the onset of S_{TI} can be forewarned has been a vital research question that has been pursued in the recent decades (Nair and Sujith 2014, Gopalakrishnan *et al* 2016, Gotoda *et al* 2014, Kobayashi *et al* 2019, Hachijo *et al* 2019, Sengupta *et al* 2020).

The present study is the first attempt to identify the onset of thermoacoustic instability that is not based on user-defined thresholds. To that end, we take a step towards identifying zones where conditions for the phase transition originate. Following the approach of Stolbova *et al* (2016), we utilize the variance of fluctuations of system observables (flame fluctuations) at different locations across the spatial domain of the thermoacoustic system to find zones with maximum growth in the variance of fluctuations, unraveling the seeds of the phase transition. Furthermore, we identify emerging long-range correlations in the flame fluctuations between these zones well before S_{TI}. Finally, we analyze the flame fluctuations at these zones to define the onset of S_{TI} and predict it in advance. We conjecture that such an approach will be helpful to
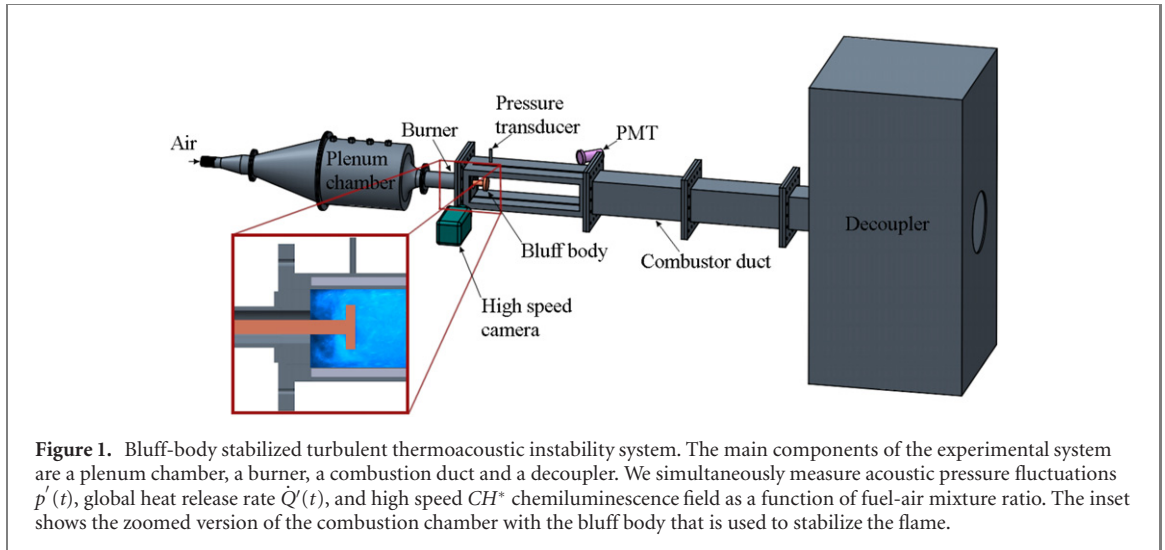
Figure 1. Bluff-body stabilized turbulent thermoacoustic instability system. The main components of the experimental system are a plenum chamber, a burner, a combustion duct and a decoupler. We simultaneously measure acoustic pressure fluctuations $p'(t)$, global heat release rate $\dot{Q}'(t)$, and high speed CH^* chemiluminescence field as a function of fuel-air mixture ratio. The inset shows the zoomed version of the combustion chamber with the bluff body that is used to stabilize the flame.

Table 1. Dimensions of the components of the test rig. All dimensions are in mm.

Component	Dimensions in mm
Plenum chamber	Diameter = 200, length = 600
Burner	Diameter = 40, length = 110
Combustion duct	Length = 1100, breadth = 90, width = 90
Decoupler	Length = 500, breadth = 500, height = 1000
Bluff body	Diameter = 47, thickness = 10
Bluff body shaft	Diameter = 16

identify the earliest manifestation of phase transitions and predict them in other engineering and natural systems as well.

2. Methods

2.1. Experimental setup

We perform experiments in a turbulent thermoacoustic system. The turbulent combustor consists mainly of a plenum chamber, a burner and a combustion chamber. The schematic of the experimental setup is shown in figure 1. The flame stabilizes inside the combustor on a flame holding device called a bluff-body shown as an inset. Air and liquefied petroleum gas (LPG: butane 60% and propane 40%) mix just before the burner. Most of the reaction occurs in the combustion chamber. Table 1 lists the dimensions of the turbulent combustor.

In this study, we vary the fuel-air mixture ratio to control the system characteristics. Mass flow controllers (MFCs) (Alicat Scientific, MCR Series) are used to control and measure the mass flow rates of air and fuel, with an uncertainty of ±0.8% of the flow rate reading in standard liters per minute (SLPM) +0.2% of the maximum flow rate of the air flow controller: 2000 SLPM. The fuel-air mixture ratio is varied linearly by increasing the air mass flow rate at a rate of 3 SLPM (with uncertainty ±0.11 SLPM) per second.

The MFCs that we utilized are proportional-integral-derivative (PID) based. The rise time of the MFCs is 100 ms. The set points of the MFC, determining the flow rates of air were regulated using voltage signals from an National Instruments Data Acquisition (NI DAQ) system. Since there is no manual operation here, repeatability of the experiments are ensured with respect to the change in flow rate of air. The mass flow rate of fuel is kept constant at 34 SLPM. An approximate thermal power for this mass flow rate of fuel is 49 kW assuming complete combustion.

We acquire $p'(t)$ using a piezoelectric pressure transducer (PCB103B02, uncertainty ±0.15 Pa). In order to record the maximum amplitude of the standing wave, the sensor is mounted at the antinode of the acoustic oscillations (25 mm distance from the backward-facing step of the combustor). The piezoelectric pressure transducer is mounted on a pressure port (T-joint) that is flush mounted on the combustor wall. To protect the transducer from excess heating from the combustor, a Teflon adapter was also used. Further, one shoulder of the T-joint was also provided with semi-infinite tubes of 10 m in length to prevent acoustic resonance within the ports and also ensure integrity of the measured signals. The mounting arrangement

does not significantly affect the analysis that we perform in the study. The voltage signals from the piezoelectric transducer were recorded utilizing a 16 bit A–D conversion card NI-6143 with an input voltage range of 5 V and a resolution of 0.15 mV.

The global CH^* chemiluminescence intensity $\dot{Q}(t)$ is captured using a photomultiplier (PMT, Hamamatsu H10722-01) mounted with a CH^* filter (435 nm $\pm$ 12 nm full width at half maximum [FWHM]) in front of it. Both $p'(t)$ and $\dot{Q}(t)$ are acquired at a sampling rate of 10 kHz. The lowest values of signal-to-noise ratio of are 11 and 28 for pressure and global heat release rate measurements respectively. Pressure and global heat release rate data from all experiments do not show a large deviation due to random errors with respect to the transition to thermoacoustic instability. At low values of $\dot{m}_{air}$, the standard deviation of the rms values across multiple experiments is 17 Pa for pressure and 0.003 arbitrary units (a.u.) for global heat release rate. At high values of $\dot{m}_{air}$, the standard deviation is (135 Pa) for pressure and 0.015 a.u. for global heat release rate. These deviations across multiple experiments do not affect the major conclusions of the study. Further, systematic errors in these measurements do not affect the analysis of fluctuations.

The spatially resolved chemiluminescence intensity ($\dot{q}(\mathbf{x}, t)$) is captured using a Phantom V12.1 high-speed camera (of spatial resolution 800 $\times$ 600 pixels) equipped with a Zeiss 100 mm lens and a CH^* filter. The images are captured at a sampling rate of 500 frames per second for a duration of 84 s. All these measurements are acquired simultaneously. Detailed descriptions of the experimental configuration, data recording systems and control systems can be found in George *et al* (2018).

3. Results

3.1. Analysis of fluctuations in the global observables

To investigate the transition from S_C to S_{TI} via S_{IN}, we perform experiments on a laboratory scale turbulent combustor (Komarek and Polifke 2010, Nair *et al* 2014, Unni *et al* 2015, Silva *et al* 2017) and acquire spatiotemporal data. Our study analyses the transition between the dynamical states by continuously varying a system parameter, the air mass flow rate ($\dot{m}_{air}$) from low to high values (Gopalakrishnan *et al* 2016, Bonciolini and Noiray 2019, Pavithran and Sujith 2021). In all the experiments, we increase $\dot{m}_{air}$ from 537 $\pm$ 8 SLPM to 780 $\pm$ 10 SLPM linearly with time. This change in $\dot{m}_{air}$ corresponds to an increase in the Reynolds number Re from $1.45 \times 10^4 \pm 428$ to $2.05 \times 10^4 \pm 555$ and a decrease in the approximate global equivalence ratio from 0.99 ($\pm$0.015) and 0.69 ($\pm$0.009). We measure two variables that represent the global state of the system: (i) the acoustic pressure fluctuations $p'(t)$ and (ii) the global heat release rate $\dot{Q}(t)$ at a data acquisition rate of 10 kHz. Meanwhile, we acquire spatiotemporal data of the local heat release rate $\dot{q}(\mathbf{x}, t)$ through high-speed imaging of CH^* radical in the combustion zone at a data acquisition rate of 500 frames per second and a spatial resolution of 800 $\times$ 600 pixels. Furthermore, we perform seven independent experiments keeping the same conditions of system parameters.

At the outset, we analyze the acoustic pressure and global heat release rate fluctuations, $p'(t)$ and $\dot{Q}'(t)$ respectively. As we increase $\dot{m}_{air}$, $p'(t)$ and $\dot{Q}'(t)$ change from aperiodic fluctuations to periodic oscillations as seen in figures 2(a) and (b) respectively. It is important to note that $p'(t)$ and $\dot{Q}'(t)$ are variables that indicate the global state of the system and are only functions of time. At the beginning of the experiment ($t = 0$) $p'(t)$ and $\dot{Q}'(t)$ are aperiodic and have low amplitude (see picture insets near $t = 5$ s). Such fluctuations show the chaotic temporal behaviour of the system at low values of $\dot{m}_{air}$ during the occurrence of S_C (Nair *et al* 2013). In contrast, as $\dot{m}_{air}$ increases, the fluctuations become periodic and grow in amplitude (picture insets at $t = 70$ s). The dominant frequency in $p'(t)$ for the large amplitude periodic oscillations, estimated by the fast Fourier transform (FFT) of a 1 s time window between $t = 79$ s and 80 s is 135 Hz (uncertainty of 0.61 Hz). Based on earlier experiments on the combustor of length 1100 mm with measurements of pressure along multiple locations of the combustor, we have found that the dominant frequency of 135 Hz is of a quarter-wave mode. For a combustor of longer length, Pawar *et al* (2017) have provided a detailed analysis on the evolution of the dominant frequency. However, neither $p'(t)$ nor $\dot{Q}'(t)$ show a demarcation between the aperiodic state and periodic state of the thermoacoustic system because of the continuous growth of periodicity.

3.2. Critical phenomena prior to the phase transition from S_C to S_{TI}

We utilize an indicator of phase transitions, the growth of variance of fluctuations (σ^2) to reveal critical phenomena in the local heat release rate fluctuations ($\dot{q}'(\mathbf{x}, t)$). In this study, $\dot{q}'(\mathbf{x}, t)$ is the only variable where we have spatial information. In fact, the spatial integral of $\dot{q}'(\mathbf{x}, t)$ gives the global measure $\dot{Q}'(t)$. We calculate σ^2 of $\dot{q}'(\mathbf{x}, t)$ at each pixel in the images (refer to appendix B for the calculation of σ^2). Following this, we estimate the composite averages of the σ^2 field by identifying the OOD for each experiment. We utilize the composite averages because the OOD need not occur at the same point in time across different
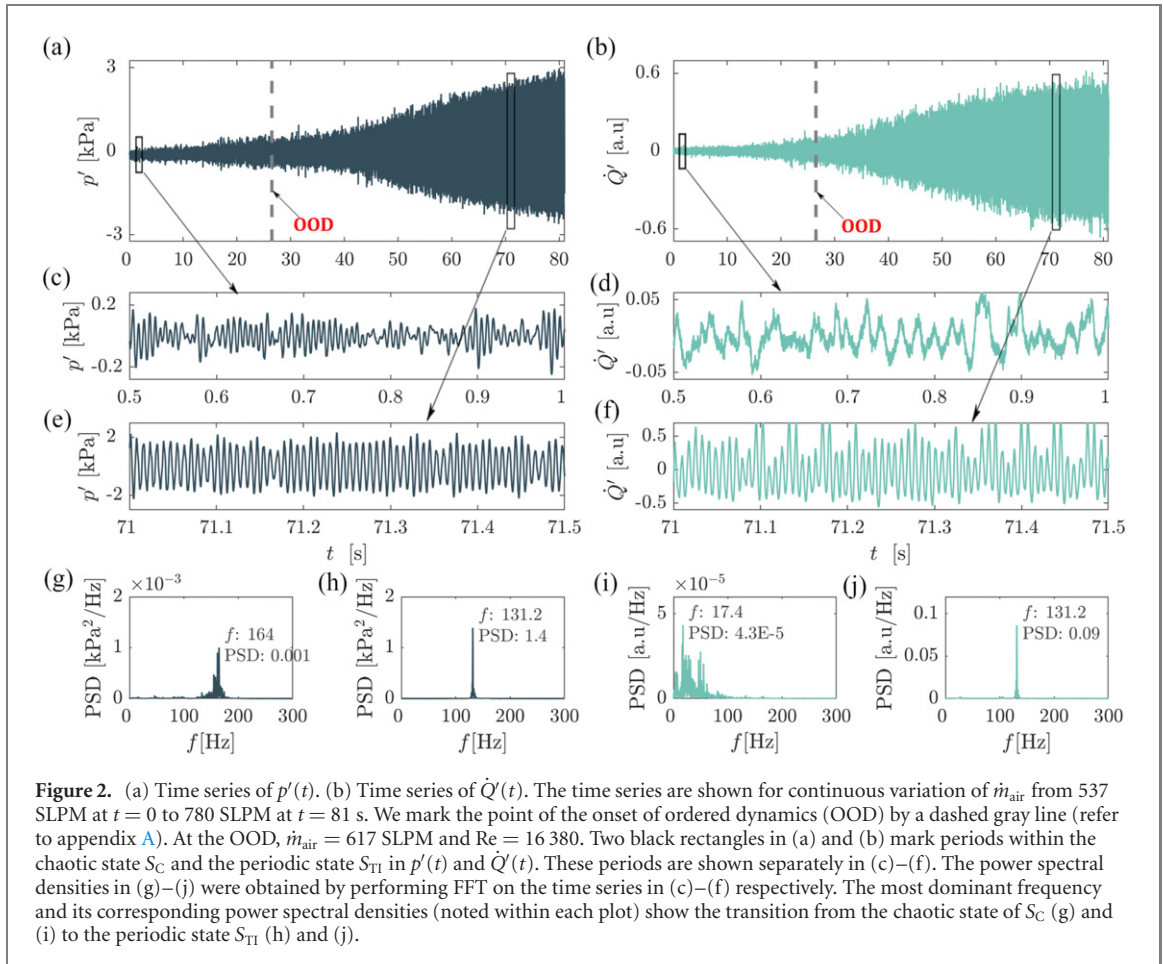
Figure 2. (a) Time series of $p'(t)$. (b) Time series of $\dot{Q}'(t)$. The time series are shown for continuous variation of $\dot{m}_{air}$ from 537 SLPM at $t = 0$ to 780 SLPM at $t = 81$ s. We mark the point of the onset of ordered dynamics (OOD) by a dashed gray line (refer to appendix A). At the OOD, $\dot{m}_{air} = 617$ SLPM and Re = 16 380. Two black rectangles in (a) and (b) mark periods within the chaotic state S_C and the periodic state S_{TI} in $p'(t)$ and $\dot{Q}'(t)$. These periods are shown separately in (c)–(f). The power spectral densities in (g)–(j) were obtained by performing FFT on the time series in (c)–(f) respectively. The most dominant frequency and its corresponding power spectral densities (noted within each plot) show the transition from the chaotic state of S_C (g) and (i) to the periodic state S_{TI} (h) and (j).
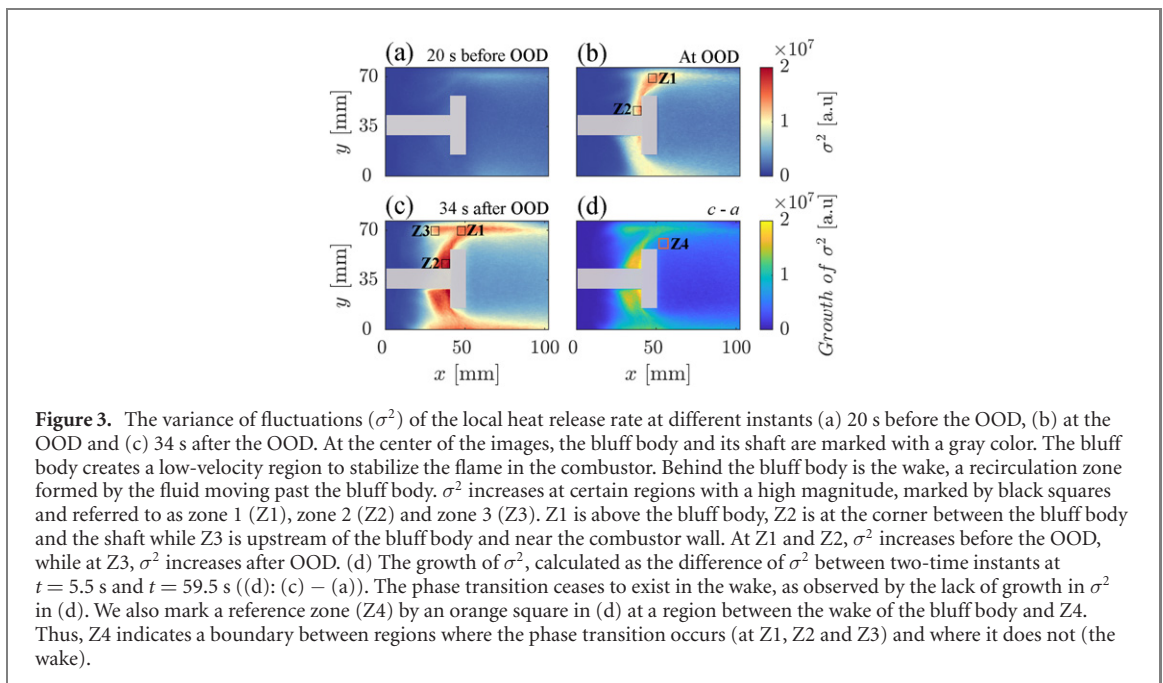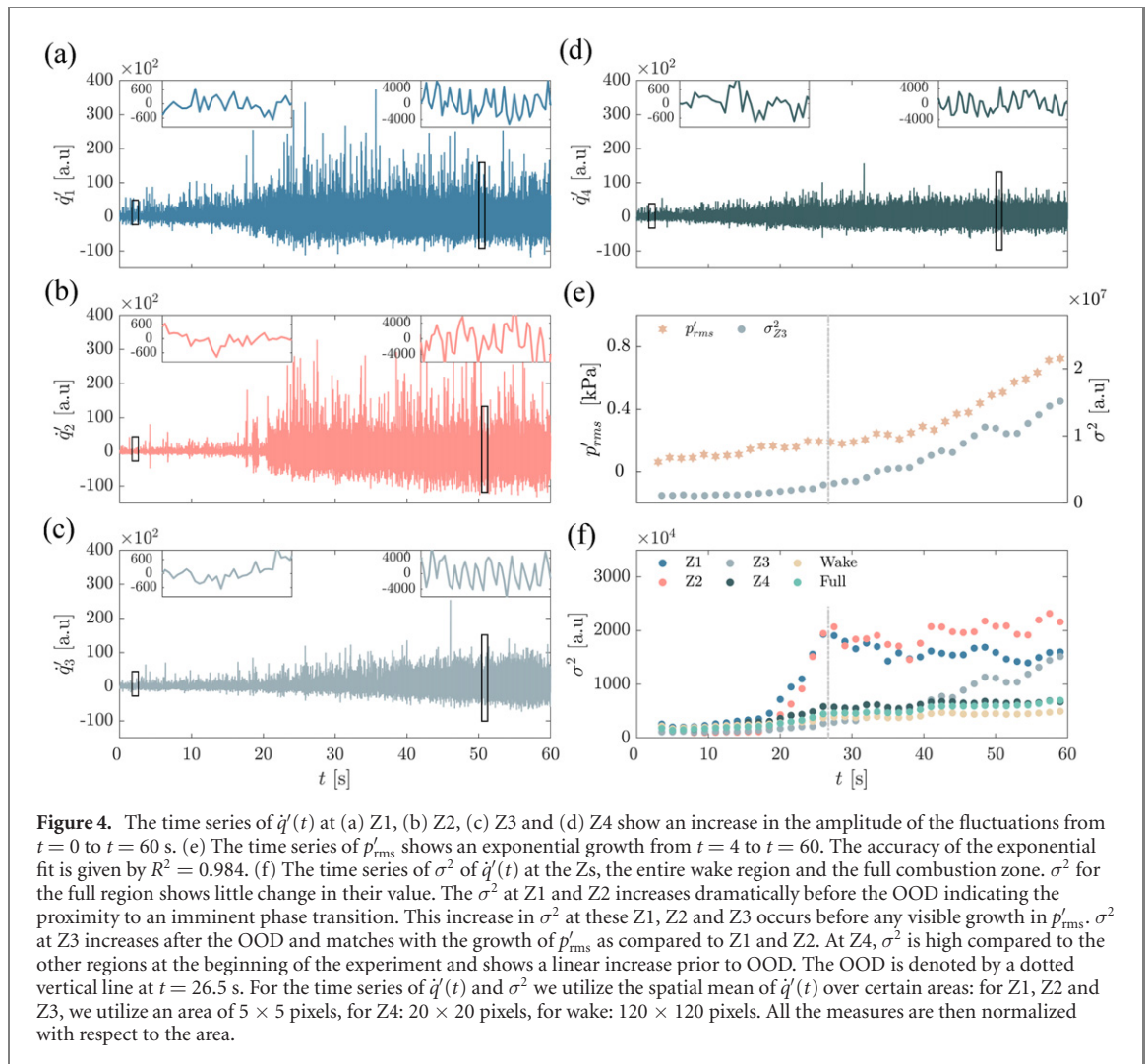

Figure 3. The variance of fluctuations (σ^2) of the local heat release rate at different instants (a) 20 s before the OOD, (b) at the OOD and (c) 34 s after the OOD. At the center of the images, the bluff body and its shaft are marked with a gray color. The bluff body creates a low-velocity region to stabilize the flame in the combustor. Behind the bluff body is the wake, a recirculation zone formed by the fluid moving past the bluff body. σ^2 increases at certain regions with a high magnitude, marked by black squares and referred to as zone 1 (Z1), zone 2 (Z2) and zone 3 (Z3). Z1 is above the bluff body, Z2 is at the corner between the bluff body and the shaft while Z3 is upstream of the bluff body and near the combustor wall. At Z1 and Z2, σ^2 increases before the OOD, while at Z3, σ^2 increases after OOD. (d) The growth of σ^2, calculated as the difference of σ^2 between two-time instants at $t = 5.5$ s and $t = 59.5$ s ((d): (c) − (a)). The phase transition ceases to exist in the wake, as observed by the lack of growth in σ^2 in (d). We also mark a reference zone (Z4) by an orange square in (d) at a region between the wake of the bluff body and Z4. Thus, Z4 indicates a boundary between regions where the phase transition occurs (at Z1, Z2 and Z3) and where it does not (the wake).

experiments. More details on the calculation of σ^2 of $\dot{q}'(\mathbf{x}, t)$, composite averages and the identification of OOD are described in appendix A. Figures 3(a)–(c) show the composite averages of σ^2 at various time instants with OOD as the time reference. The composite averages show a localized increase in σ^2 as the system approaches OOD.

The non-uniform distribution of σ^2 before OOD occurs due to non-uniform flow conditions associated with the geometry of the bluff body and the resultant non-uniform heat release rate. Figure 3(a) shows that

Figure 4. The time series of $\dot{q}'(t)$ at (a) Z1, (b) Z2, (c) Z3 and (d) Z4 show an increase in the amplitude of the fluctuations from $t = 0$ to $t = 60$ s. (e) The time series of p'_{rms} shows an exponential growth from $t = 4$ to $t = 60$. The accuracy of the exponential fit is given by $R^2 = 0.984$. (f) The time series of σ^2 of $\dot{q}'(t)$ at the Zs, the entire wake region and the full combustion zone. σ^2 for the full region shows little change in their value. The σ^2 at Z1 and Z2 increases dramatically before the OOD indicating the proximity to an imminent phase transition. This increase in σ^2 at these Z1, Z2 and Z3 occurs before any visible growth in p'_{rms}. σ^2 at Z3 increases after the OOD and matches with the growth of p'_{rms} as compared to Z1 and Z2. At Z4, σ^2 is high compared to the other regions at the beginning of the experiment and shows a linear increase prior to OOD. The OOD is denoted by a dotted vertical line at $t = 26.5$ s. For the time series of $\dot{q}'(t)$ and σ^2 we utilize the spatial mean of $\dot{q}'(t)$ over certain areas: for Z1, Z2 and Z3, we utilize an area of 5×5 pixels, for Z4: 20×20 pixels, for wake: 120×120 pixels. All the measures are then normalized with respect to the area.

σ^2 at all regions is low much before the OOD. However, with an increase in $\dot{m}_{air}$ and near OOD, σ^2 increases particularly at two zones, referred to as Z1 and Z2 as shown in figure 3(b). Additionally, at these locations, σ^2 remains high relative to other regions long after the OOD (see figure 3(c)). On the other hand, figures 3(a)–(c) exhibit that the recirculation zone behind the bluff body has low σ^2 because of aperiodic fluctuations (shown later in figure 4(d)). After the OOD, in figure 3(c) we observe a third zone, Z3, which exhibits an increase in σ^2. In general, figure 3(d) reveals that Z1, Z2 and Z3 exhibit the highest growth of σ^2. We find that prior to OOD the growth of variance of fluctuations at these locations we consider to be seeds of the transition is indeed statistically significant with *p*-value < 0.01 (see appendix E for details). We mark a region Z4 by an orange square between Z1 and the wake region in figure 3(d), which shows low growth in σ^2. Due to the combustor's axisymmetric profile with respect to the shaft, we have similar dynamics below the shaft. Thus, the growth in σ^2 of the flame fluctuations allows us to locate Z1, Z2 and Z3, out of which Z1 and Z2 exhibit the earliest manifestation of the onset of thermoacoustic instability.

The increase of σ^2 within the confined reactive system indicates that critical phenomena occurs at selected zones of the flame enroute to S_{TI}. The growth of σ^2 at these zones remain high for independent experiments conducted at different combustor lengths, position of bluff body, mass flow rates of fuel, rate of increase of mass flow rate of air etc. The geometry of the system gives special importance to different regions within the confined reactive system. For instance, flame stabilization occurs at the bluff body. The corner between the shaft and the bluff body where Z2 is located provides a low-velocity region, vital for flame stabilization (Lieuwen and Yang 2005). This region is directly in line with the incoming bulk flow of fresh reactants. Z1 is a location of high heat release rate fluctuations after the impingement of large-scale flow structures while Z3 is at the region where the largest size of the flow structure exists before impingement (George *et al* 2018). Even though the flame is spatially extended in the confined reactive system, there may be certain zones where the increase in local fluctuations appear regularly due to the geometry of the system. Thus, the fact that criticality does not appear in all regions within the combustor is not surprising.

3.3. Local increase in variance of fluctuations as an indicator of the phase transition

The increase in the variance of fluctuations of $\dot{q}'(t)$ at Z1 and Z2 indicates an early manifestation of the phase transition from the aperiodic state to the periodic state. Figures 4(a)–(c) show the evolution from aperiodic dynamics to periodic oscillations at Z1, Z2 and Z3 respectively. At Z1 and Z2, $\dot{q}'(t)$ has a low amplitude and is aperiodic before the OOD, while near the OOD, the amplitude of $\dot{q}'(t)$ increases at both Z1 and Z2. In fact, the increase in amplitude of $\dot{q}'(t)$ manifests as a localized emergence of periodic flame oscillations at these regions. This increase in $\dot{q}'(t)$ is evident from the substantial increase in σ^2 at these locations, seen in figure 4(f). The high $\dot{q}'(t)$ at Z2 can be attributed to the flapping of the shear layer which is one of the underlying mechanisms of S_{TI} (Premchand *et al* 2019). The maximum value of σ^2 at Z1 and Z2 occurs near the OOD, indicating that they form a pair of zones wherein critical phenomena occurs first.
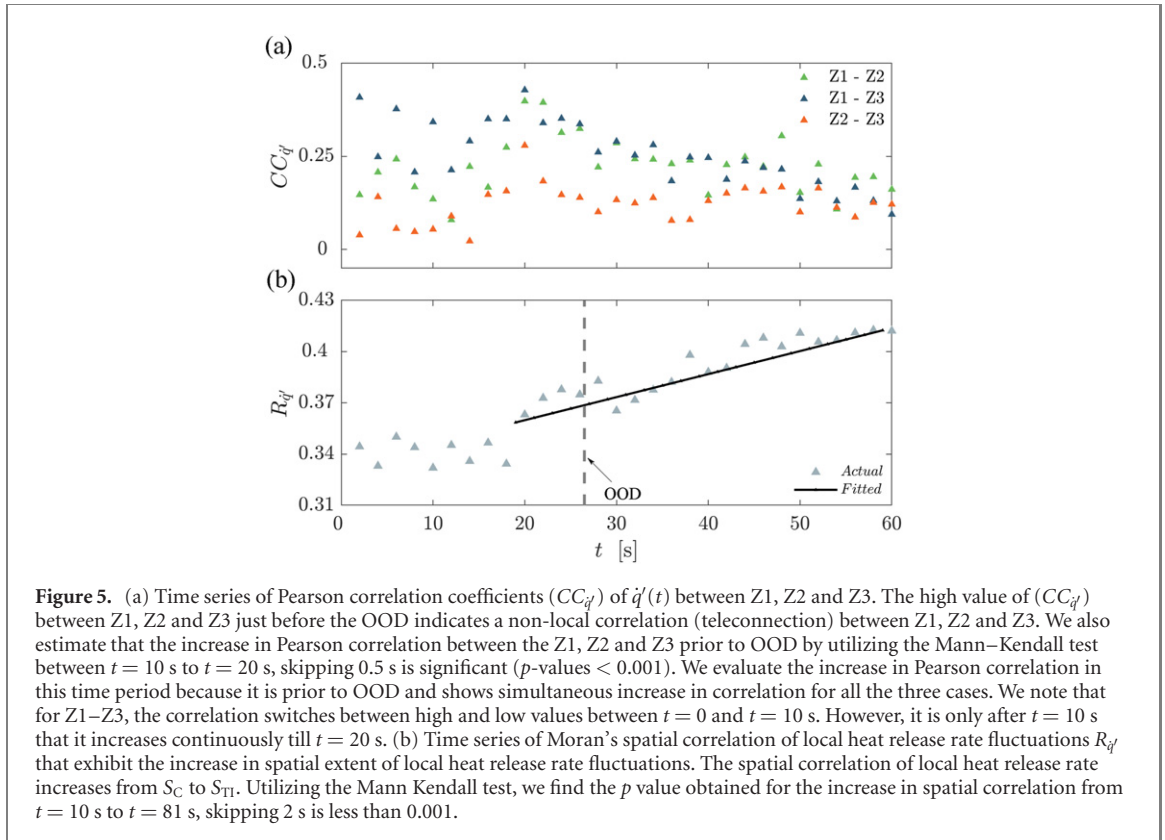
On the other hand, this critical phenomena is neither seen in global measures of $p'(t)$ and $\dot{Q}'(t)$ nor in σ^2 at other regions of the combustor prior to the OOD. In particular, figures 4(e) and (f) indicate that both the p'_{rms} (root mean square of the acoustic pressure fluctuations) and σ^2 of the full combustion zone show a negligible increase before the OOD. Hence, there is no indication of a phase transition in the global dynamics. At the same time, local flame fluctuations at Z1 and Z2 indicate an early manifestation of the transition from S_C to S_{TI}. In contrast, σ^2 at the wake remains low for the entire duration of the experiment. The local flame fluctuations in the wake may be aperiodic or periodic with low strength of fluctuations. Figures 4(a), (b) and (d) indicate that at Z4, the growth of $\dot{q}'(t)$ is relatively small compared to that at Z1 and Z2.

Even though the importance of Z3 during S_{TI} due to the emergence of large-scale coherent vortices is clear, Z3 does not show the earliest indication of the phase transition. The amplitude of $\dot{q}'(t)$ at Z3 grows gradually with increase in $\dot{m}_{\text{air}}$. In fact, figure 4(e) exhibits that σ^2 at Z3 closely matches the growth of p'_{rms} in comparison to σ^2 at Z1 and Z2. This close match of the variation of σ^2 at Z3 and p'_{rms} is expected because of the influence of impingement of large-scale coherent flow structures formed from spatial organization of small-scale vortices during S_{TI} (Poinsot *et al* 1987, Yu *et al* 1991, Hong *et al* 2013, George *et al* 2018). On the other hand, at S_C, such spatial organization does not occur, resulting in low amplitude aperiodic flame fluctuations. Thus, although $\dot{q}'(t)$ at Z3 is high during S_{TI}, the growth in σ^2 is low before the OOD. However, the localized increase in periodic fluctuations of $\dot{q}'(t)$ at Z1 and Z2 may eventually enhance the mutual feedback between $p'(t)$ and $\dot{q}'(\mathbf{x}, t)$, pushing the state of the system from S_C to S_{TI}.

3.4. Teleconnections within the flame near the phase transition

Correlation analysis shows that Z1, Z2 and Z3 indicate a localized increase in long-range connections or teleconnections between them before the OOD. We utilize Pearson correlation (Lee Rodgers and Nicewander 1988) and Moran's spatial correlation (Moran 1950) to analyze the correlations within the combustion zone (more details in appendices C and D). Spatial order emerges in the flame and flow dynamics from S_C to S_{TI} (George *et al* 2018, Unni *et al* 2018). Pearson correlation coefficient of $\dot{q}'(t)$ ($CC_{\dot{q}'}$) between Z1, Z2 and Z3 shown in figure 5(a) reveals non-local and long-range connections between them near the OOD. In fact, we observe that $CC_{\dot{q}'}$ between Z1, Z2 and Z3 increases prior to the OOD. The correlation between these regions is statistically significant with p-values < 0.001 (see appendix F for details). Rocha *et al* (2018) showed that an interaction between tipping elements can result in cascading effects and a phase transition in the global dynamics. Clearly, the increase in $CC_{\dot{q}'}$ corresponds to the increase in σ^2 at both Z1 and Z2. Such an increase in $CC_{\dot{q}'}$, especially before any appreciable change in the global measures of p'_{rms} and $\dot{Q}'_{\text{rms}}$, indicates an emerging teleconnection between Z1, Z2 and Z3 before the OOD. In a recent study Godavarthi *et al* (2020) utilized non-identical Rössler oscillators and a chaotic Van der Pol oscillator to represent the spatially resolved heat release rate and the acoustic pressure respectively. They showed that with increase in the coupling strength, the acoustic pressure fluctuations changed from a chaotic state to a periodic state via intermittency. The increase in correlation of the local heat release rate near the zones Z1 and Z2 mirrors the change from asynchronized chaos to generalized synchronization observed by Godavarthi *et al* (2020).

On the contrary, beyond the OOD, the correlation between these zones decrease, when one may expect it to increase because the amplitude of the periodic oscillations continues to grow after the OOD (refer figure 2). But, we also observe that the spatial extent of the correlated behaviour increases as the system approaches S_{TI}. In fact, in figure 5(b), we observe an increase in spatial correlation of the local heat release rate fluctuations $R_{\dot{q}'}$ with increase in $\dot{m}_{\text{air}}$ (more details on calculation of $R_{\dot{q}'}$ is in appendix D). $R_{\dot{q}'}$ fluctuates around 0.34 before exhibiting a continuous increase in $R_{\dot{q}'}$ after $t = 18$ s. Thus, even though after the OOD the temporal correlation between the zones Z1, Z2 and Z3 decreases, the spatial correlation in the heat release rate fluctuations within the entire flame zone increases.

Figure 5. (a) Time series of Pearson correlation coefficients ($CC_{\dot{q}'}$) of $\dot{q}'(t)$ between Z1, Z2 and Z3. The high value of ($CC_{\dot{q}'}$) between Z1, Z2 and Z3 just before the OOD indicates a non-local correlation (teleconnection) between Z1, Z2 and Z3. We also estimate that the increase in Pearson correlation between the Z1, Z2 and Z3 prior to OOD by utilizing the Mann–Kendall test between $t = 10$ s to $t = 20$ s, skipping 0.5 s is significant (p-values < 0.001). We evaluate the increase in Pearson correlation in this time period because it is prior to OOD and shows simultaneous increase in correlation for all the three cases. We note that for Z1–Z3, the correlation switches between high and low values between $t = 0$ and $t = 10$ s. However, it is only after $t = 10$ s that it increases continuously till $t = 20$ s. (b) Time series of Moran's spatial correlation of local heat release rate fluctuations $R_{\dot{q}'}$ that exhibit the increase in spatial extent of local heat release rate fluctuations. The spatial correlation of local heat release rate increases from S_C to S_{TI}. Utilizing the Mann Kendall test, we find the p value obtained for the increase in spatial correlation from $t = 10$ s to $t = 81$ s, skipping 2 s is less than 0.001.

3.5. Identification of critical conditions and predicting the phase transition in advance

Analysis of the strength of the local flame fluctuations reveal a crucial temporal relationship between Z2 and Z4. As we utilize a sliding window approach to obtain the fluctuations of the heat release rate, the rms of these fluctuations: $\dot{q}'_{rms}$ becomes equivalent to the square root of σ^2. Nevertheless, since the rms value has traditionally been used to define the strength of the flame fluctuations, we utilize the rms of $\dot{q}'(\mathbf{x}, t)$ to define the relationship between Z2 and Z4. Notably, even though the utilization of $\dot{q}'_{rms}$ is not new, phenomena of emerging correlations or synchronization of local heat release rate fluctuations has been investigated only recently (Mondal *et al* 2017, George *et al* 2018). Further, $\dot{q}'_{rms}$ has traditionally been utilized to estimate only the mean field conditions of the system. It is only recently that σ^2 has been employed on temporal fluctuations to obtain early warning signals in thermoacoustic systems (Gopalakrishnan *et al* 2016). However, utilizing the increase in the rms (or σ^2) of spatial measures has never been explored to identify the phase transition nor provide early warning measures.

Figure 6(a) shows that $\dot{q}'_{rms}$ at Z2 abruptly shifts from 800 a.u. at $\dot{m}_{air} = 580$ SLPM ($t = 14$ s) to 4000 a.u. at $\dot{m}_{air} = 610$ SLPM ($t = 24$ s), indicating a high magnitude transition. At other locations, the transition is not as sharp as that at Z2. Such a high magnitude transition is a key feature of a phase transition from one state to another state. Further, as seen earlier in figure 3(d), the earliest manifestation of critical phenomena also occurs at Z1 and Z2 wherein Z2 shows the highest growth in σ^2 of the local flame fluctuations. These features of the phase transition at Z2 makes it an ideal candidate to demarcate the chaotic state (S_C) and the periodic state (S_{TI}). On the other hand, $\dot{q}'_{rms}$ at Z4 is slightly higher than at Z2 during the state of S_C and increases with $\dot{m}_{air}$. $\dot{q}'_{rms}$ at Z4 and Z2 intersect before OOD near the mid point between the low values and high values of $\dot{q}'_{rms}$ at Z2. This intersection of $\dot{q}'_{rms}$ at Z2 and Z4 occurs for all the seven experiments prior to the OOD. For the experimental data shown in figure 6(a), the intersection occurs at $\dot{m}_{air} = 597$ SLPM, where $\dot{q}'_{rms} = 1839$ a.u. We denote $\dot{q}'_{rms}$ at the point of intersection as $\dot{q}'^i_{rms}$. Indeed, there are some fluctuations near the intersection because of the turbulent flow field, which pushes the local dynamics back and forth between the chaotic state (low $\dot{q}'_{rms}$) and large amplitude periodic state (high $\dot{q}'_{rms}$) due to its inherent stochasticity. Nevertheless, we consider the last intersection to denote $\dot{q}'^i_{rms}$.

We define the set of critical conditions under which a transition to thermoacoustic instability begins: critical zones and a critical value in the heat release rate fluctuations. There are two critical zones: Z2 and Z4. While Z2 exhibits the earliest manifestation of critical phenomena and the highest increase in fluctuations, Z4 shows a faster rate of growth of $\dot{q}'_{rms}$ on the eve of the onset of S_{TI}. The onset of S_{TI} happens when the magnitudes of $\dot{q}'_{rms}$ at these two zones reach the same level. Utilizing the point of intersection $\dot{q}'^i_{rms}$, we define the critical value in the heat release rate fluctuations. We select four out of the seven experiments
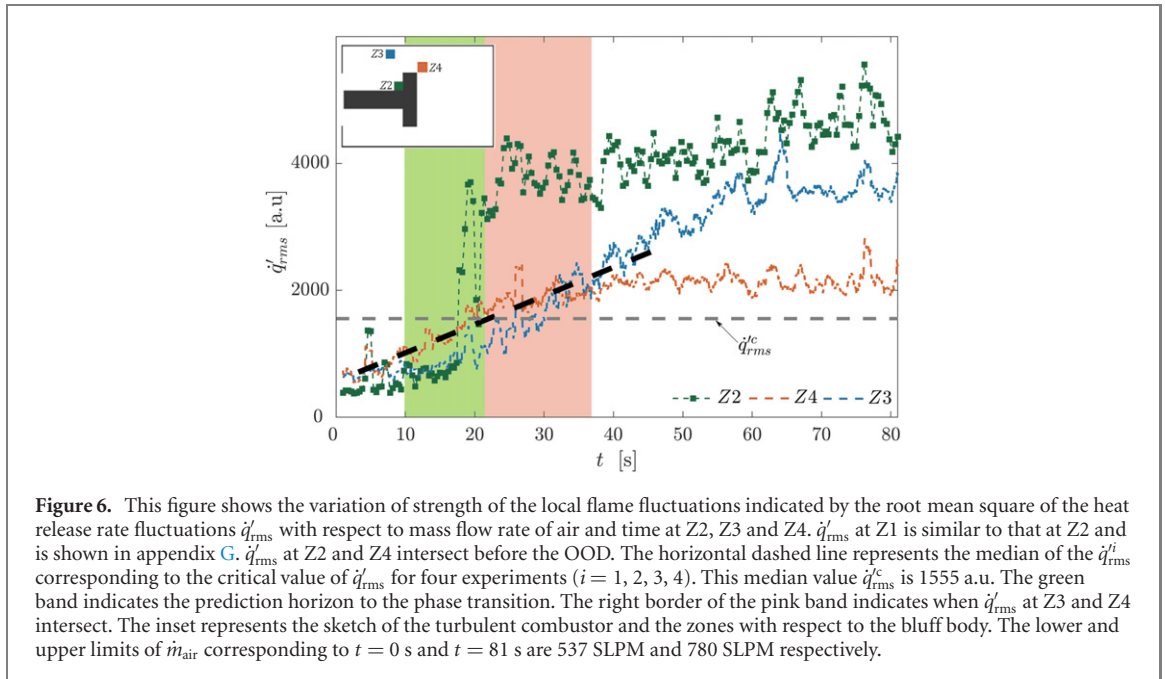
Figure 6. This figure shows the variation of strength of the local flame fluctuations indicated by the root mean square of the heat release rate fluctuations $\dot{q}'_{rms}$ with respect to mass flow rate of air and time at Z2, Z3 and Z4. $\dot{q}'_{rms}$ at Z1 is similar to that at Z2 and is shown in appendix G. $\dot{q}'_{rms}$ at Z2 and Z4 intersect before the OOD. The horizontal dashed line represents the median of the $\dot{q}'^i_{rms}$ corresponding to the critical value of $\dot{q}'_{rms}$ for four experiments ($i = 1, 2, 3, 4$). This median value $\dot{q}'^c_{rms}$ is 1555 a.u. The green band indicates the prediction horizon to the phase transition. The right border of the pink band indicates when $\dot{q}'_{rms}$ at Z3 and Z4 intersect. The inset represents the sketch of the turbulent combustor and the zones with respect to the bluff body. The lower and upper limits of $\dot{m}_{air}$ corresponding to $t = 0$ s and $t = 81$ s are 537 SLPM and 780 SLPM respectively.

Table 2. Utilizing the interconnected zones show high accuracy in predicting the phase transition. Key: $\dot{m}_a$—mass flow rate of air at which $\dot{q}'_{rms}$ of Z2 crosses Z4 for the experiment; $\dot{m}_p$—predicated value of air mass flow rate in SLPM utilizing the regression line from the time series at Z4 and the critical value $\dot{q}'^c_{rms}$; δ—standard error in percentage and is given as ($\dot{m}_a - \dot{m}_p$)/$\dot{m}_a$. The discrepancy between $\dot{m}_a$ and $\dot{m}_p$ is within the uncertainty limits of the controller at these flow rates (± 9 SLPM).

Sl. No.	$\dot{m}_a$	$\dot{m}_p$	δ (%)
1	587 SLPM	585 SLPM	0.34
2	596 SLPM	590 SLPM	1.00
3	599 SLPM	601 SLPM	−0.33

to make a training set. We choose the median of $\dot{q}'^i_{rms}$ from these four experiments to define the critical value of heat release rate fluctuations: $\dot{q}'^c_{rms} = 1555$ a.u. Once the strength of the local heat release rate fluctuations at Z2 increases beyond $\dot{q}'^c_{rms}$, these fluctuations do not return to their low amplitude chaotic state but continue to grow in amplitude and periodicity en route to S_{TI} for all the experiments. Nair and Sujith (2014) proposed a user-defined threshold of 0.1 for the Hurst exponent (H) of $p'(t)$ to demarcate the state of S_{TI} from S_C. Notably, H decreases to 0.1 at the intersection point of Z2 and Z4 (see appendix G for details). This feature further substantiates our view that the occurrence of the critical phenomena at Z2 and Z1 locally indicates the onset of thermoacoustic instability.

Subsequently, we utilize this $\dot{q}'^c_{rms}$ (marked by the gray dashed line in figure 6(a)) to predict the onset in the other three experiments. At Z4, the $\dot{q}'_{rms}$ increases linearly till the OOD that may be attributed to the gradual increase in the frequency of vortex shedding from the tip of the bluff body depending on $\dot{m}_{air}$. We attempt to predict the onset by making a linear fit of $\dot{q}'_{rms}$ at Z4 for each of the three experiments and identify where the linear fit intersects $\dot{q}'^c_{rms}$ (see dashed black line in figure 6(a)). Table 2 shows the results from the prediction. The second column of table 2 represents the mass flow rate of air $\dot{m}_a$ where the intersection between $\dot{q}'_{rms}$ at Z2 and Z4 occur. The third column shows the predicted air mass flow rate ($\dot{m}_p$) obtained from the linear fit and $\dot{q}'^c_{rms}$. The discrepancy between $\dot{m}_a$ and $\dot{m}_p$ is within 1%, for the three test cases. These discrepancies are within the uncertainty limits of the MFC. In general, this methodology predicts the earliest manifestation of the onset 11 s in advance, which corresponds to a change of $\dot{m}_{air} = 33$ SLPM.

The choice of the reference zone Z4 to define the critical point and predict the phase transition is not arbitrary. Unlike the interconnected zones, the $\dot{q}'_{rms}$ at Z4 increases from the beginning of the experiment.

Once the phase transition occurs, $\dot{q}'_{\text{rms}}$ at Z4 saturates to a value close to 2000 a.u. On the other hand, at the wake, the $\dot{q}'_{\text{rms}}$ always remains low while regions within the area spanned by Z1 and Z2 show a phase transition near the OOD (not shown here). Meanwhile, at regions near Z3, the large magnitude phase transition occurs slower, as indicated by the slow increase in $\dot{q}'_{\text{rms}}$ at Z3. Hence, Z4, is a special location, representing a boundary between the zones wherein the earliest manifestation of phase transition occurs (Z1 and Z2) and where the phase transition ceases to exist (wake). The intersection point between Z2 and Z4 means an equalization of the strength of fluctuations at the stagnation point and the vortex shedding region. Changes in the area selected for Z4 (within the wake region) do not significantly affect the value of $\dot{q}'^{c}_{\text{rms}}$. Large changes in the selection of Z4 would result in either $\dot{q}'^{c}_{\text{rms}}$ being too high, which is inappropriate for the definition of critical value in this case, or too low, which may lie within the vicinity of local fluctuations at Z2.

Interestingly, $\dot{q}'_{\text{rms}}$ at Z3 and Z4 also intersect near the mid point between the low values and high values of $\dot{q}'_{\text{rms}}$ at Z3. This intersection occurs at $\dot{m}_{a} = 645$ SLPM, marked by the right border of the vertical pink band. We observe that at this point, the amplitude of the pressure oscillations reach 25% of the maximum observed amplitude, giving us an insight to how early the onset is. In fact, this intersection occurs 16 s later than the earliest manifestation of the phase transition at Z1 and Z2. Z3 shows high $\dot{q}'_{\text{rms}}$ when large-scale coherent flow structures emerge. This shows clear evidence that the earliest manifestation of the phase transition occurs in advance to the emergence of large-scale coherent structures. Such features of Z4 and its relationship with Z2 motivates its use in defining the onset of thermoacoustic instability and predicting it.

We hypothesize that the features at Z1, Z2, Z3 and Z4 would remain the same irrespective of the changes in the experimental conditions such as different fuel flow rates, different rate of change of mass flow rate of air. The features persist due to following reasons. Firstly, at Z1, which is just above the bluff body, high heat release rate occurs after impingement of the large-scale flow structures (George *et al* 2018). Secondly, at Z3, which is located upstream of the bluff body, large-scale flow structures emerging during the state of thermoacoustic instability is ubiquitous and has been reported in multiple studies in the same experimental setup (George *et al* 2018, Raghunathan *et al* 2020). Finally, the divergent flow at Z2 (corner of bluff body and shaft) and the vortex shedding at Z4 (between the wake and Z1) are imposed by the geometry of the bluff body. Hence, we expect critical phenomena to occur locally at Z1 and Z2 before the phase transition, irrespective of changes in experimental conditions.

4. Discussion and conclusion

We have presented comprehensive experimental evidence on identifying two interconnected zones—seeds of the phase transition in a turbulent reactive flow system that point to the earliest manifestation of the phase transition. First, we have unraveled those zones, where the earliest manifestation of the onset of phase transition appears, utilizing the increase in the variance of local fluctuations of the flame. Second, the emergence of long-range correlations between these zones prior to the onset of the phase transition has been found. Next, we have identified the critical value of the heat release rate fluctuations at these interconnected zones. These findings enable us to identify the onset of a phase transition from a chaotic state to a periodic state, which in our case is the onset of thermoacoustic instability. Notably, all precursors which have been shown in recent decades are indicators of an impending thermoacoustic instability. To the best of the authors' knowledge, a prediction of when the onset will occur has not been shown in any experimental, numerical or analytical study to date. Our result opens promising perspectives for predicting the onset of transitions in complex systems wherein acquisition of spatiotemporal data is possible.

Previously, Stolbova *et al* (2016) revealed tipping elements in the Indian monsoon system by analyzing observational data of atmospheric variables, utilizing the time series at the tipping elements. These tipping elements allowed predicting the onset of the monsoon with large lead times. It has been proven to be successful retrospectively in the prediction of future monsoons for five consecutive years since its introduction in 2016 (Ludescher *et al* 2021). We have adapted the tipping elements approach for turbulent combustor and have developed it further for the case of thermoacoustic instability. This methodology allows to predict the earliest manifestation of the onset before it appears. Importantly, the methodology that we have used to identify the zones where the earliest manifestation of the onset appears do not need detailed information of the influential processes that drive the transition. In fact, the earliest manifestation of the phase transition is found only by utilizing the criterion, which is the growth in the variance of fluctuations of certain system variables. The evidence from both observational data analysis and our experimental results shows the applicability of the methodology for various complex systems and demonstrate the predictive power with sufficient lead times.

The developed methodology is applicable to multidimensional complex systems exhibiting phase transitions. The only prerequisite is to have spatial data of a system variable that shows the phase transition.

For more complex 3D flames, the identification of seeds of a phase transition may require acquisition of spatial data in x, y and z directions, which is more challenging. On the other hand, in simpler systems such as the Rijke tube, the onset is well defined by the Hopf point. Thus, the usefulness of the methodology in thermoacoustics would lie in more complex geometries with turbulent and non-compact flames wherein the acquisition of spatial information is of value and possible.

The suppression of the onset of the phase transition may open new perspectives for 'greener' operations. We hypothesize that the interconnected zones perform as bridges to ordered dynamics that initiate positive feedbacks within the system, necessary for the phase transition to occur. Suppressing the spatiotemporal organization in such zones should break a pathway to S_{TI}. In general, most control strategies intend to destroy large-scale coherent flow structures that exist at S_{TI}. However, we have revealed that the onset of S_{TI} at the interconnected zones Z1 and Z2 occurs even before the emergence of these large-scale coherent structures. The growth of σ^2 at these zones remain high for independent experiments conducted at different combustor lengths, position of bluff body, mass flow rates of fuel, rate of increase of mass flow rate of air etc.

Our findings suggest that it may be necessary and useful to implement control strategies at this onset of S_{TI} which appears much before the large amplitude oscillations of p' occur. The revealed interconnections between these zones suggests a promising way to suppress the phase transition by disrupting the linkage between them and thus block a pathway to S_{TI}. Further, the question of whether suppressing critical phenomena at the interconnected zones can suppress thermoacoustic instability also remains an open question. Pursuing this research question is important for developing passive control strategies. Preliminary experiments show that suppression of thermoacoustic instability close to 90% is possible by adopting such a strategy, but this is for future study. Thus, our study provides a very-much-needed understanding of experimental evidence showing the special role of the seeds of phase transition (Frenkel 2006) that mark the earliest manifestation of the transition to thermoacoustic instability, which allow us to define the onset of thermoacoustic instability. This is a crucial step for 'greener' operations.
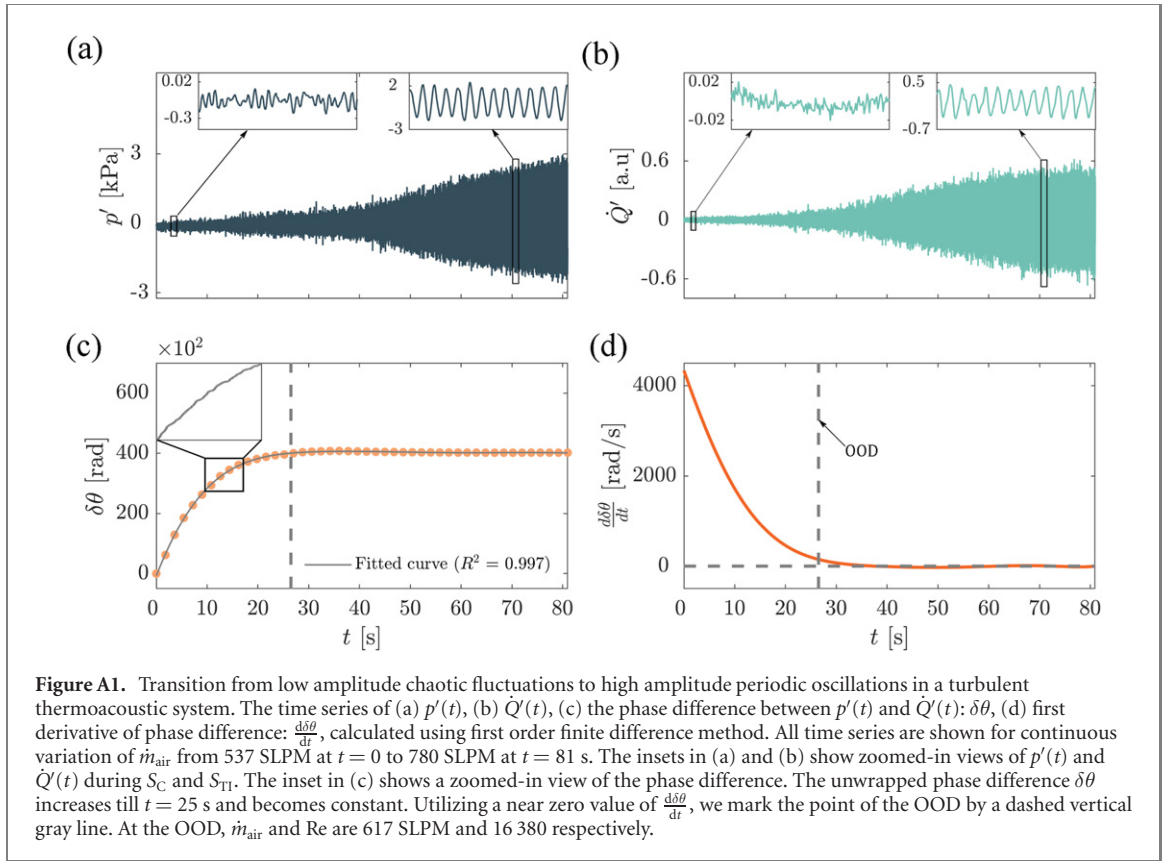
Acknowledgments

Data availability statement

The data that support the findings of this study are available upon reasonable request from the authors.

Appendix A. Estimating the composite averages of σ^2 field based on identifying the onset of ordered dynamics (OOD)

We analyze the phase difference between $p'(t)$ and $\dot{Q}'(t)$ to estimate a common reference between the multiple experiments since the individual global measures do not reveal a period wherein the transition occurs. We calculate the instantaneous phase ($\delta\theta$) between $p'(t)$ and $\dot{Q}'(t)$ using Hilbert transform (HT) (Madjarova *et al* 2003). At first, we compute the phase and amplitude of $p'(t)$ and $\dot{Q}'(t)$ individually using HT. Then the relative phase between $p'(t)$ and $\dot{Q}'(t)$ is calculated as the difference between the computed phase of those signals. In general, the relative phase between two signals is bounded in an interval $[-180\ 180]$. However, here, we unwrapped $\delta\theta$ obtained from HT to visualize how $\delta\theta$ continuously changes during the transition from combustion noise to thermoacoustic instability.

Figure A1(c) shows the continuously changing phase difference ($\delta\theta$) from $t = 0$ s, which begins to converge to an asymptotic value near $t = 25$ s. Previous studies have shown that as the $p'(t)$ and $\dot{Q}'(t)$

Figure A1. Transition from low amplitude chaotic fluctuations to high amplitude periodic oscillations in a turbulent thermoacoustic system. The time series of (a) $p'(t)$, (b) $\dot{Q}'(t)$, (c) the phase difference between $p'(t)$ and $\dot{Q}'(t)$: $\delta\theta$, (d) first derivative of phase difference: $\frac{d\delta\theta}{dt}$, calculated using first order finite difference method. All time series are shown for continuous variation of $\dot{m}_{air}$ from 537 SLPM at $t = 0$ to 780 SLPM at $t = 81$ s. The insets in (a) and (b) show zoomed-in views of $p'(t)$ and $\dot{Q}'(t)$ during S_C and S_{TI}. The inset in (c) shows a zoomed-in view of the phase difference. The unwrapped phase difference $\delta\theta$ increases till $t = 25$ s and becomes constant. Utilizing a near zero value of $\frac{d\delta\theta}{dt}$, we mark the point of the OOD by a dashed vertical gray line. At the OOD, $\dot{m}_{air}$ and Re are 617 SLPM and 16 380 respectively.

become periodic, their phase difference becomes constant (Pawar *et al* 2017, Chen *et al* 2021). Next, we calculate the first derivative of $\delta\theta$: $\frac{d\delta\theta}{dt}$, which is shown in figure A1(d). As the phase difference becomes constant, the first derivative of the phase difference will approach zero. We mark the time instant wherein the $\frac{d\delta\theta}{dt}$ reaches 99.99% of the difference between the largest positive value and zero, and refer to it as the OOD. For experimental data shown in figure A1, we identify the OOD at $t = 26.5$ s where $\dot{m}_{air}$ is 617 SLPM. The same approach is followed to obtain OOD for the other experiments. Subsequently, we estimate averages across the seven experiments with respect to OOD as the reference point from each experiment. These averages, referred to as composite averages are shown in figure 3 for σ^2 fields at different instants of time with respect to OOD. We utilize these composite averages to standardize σ^2 prior to the OOD.
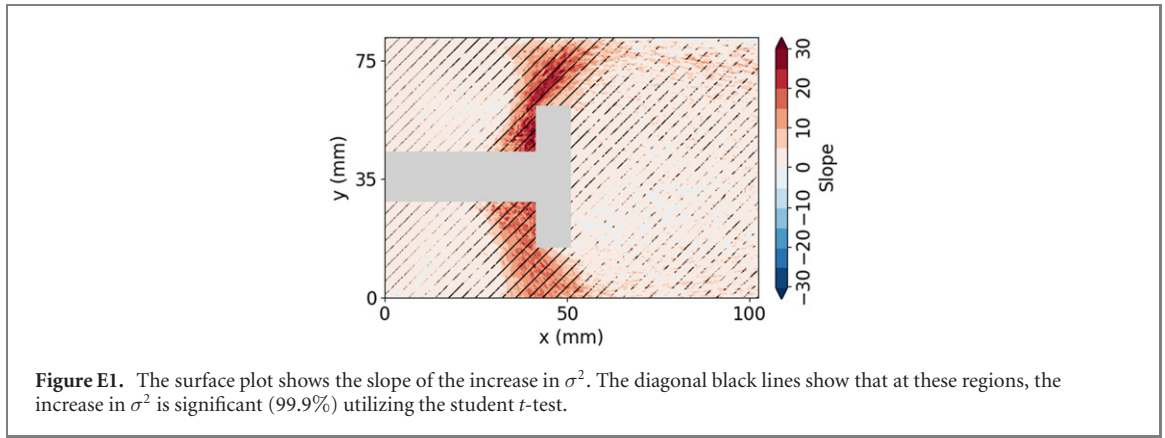
Appendix B. Calculation of variance of fluctuations of local heat release rate.

We calculate the variance of fluctuations σ^2 of $\dot{q}(\mathbf{x}, t)$ at each pixel for a time period of $w = 3.5$ s wherein the fluctuations are calculated based on a moving average of $w_s = 0.04$ s. d refers to the time instant at which the calculation is performed.

$$\sigma^2(\dot{q}, d, w, w_s) = \sum_{k=1}^{w} \frac{\left[\dot{q}(\text{OOD} - d - k) - \sum_{i=1}^{w_s} \frac{\dot{q}(\text{OOD}-d-k-i)}{w_s} \right]^2}{w}. \tag{B.1}$$

For example, assuming OOD is at 25 s, to calculate σ^2 20 s (d) before the OOD, we utilize the fluctuations from $t = 1.5$ s to $t = 5$ s.

In many cases, absolute values are crucial to understand certain phenomena and calibration of the measuring devices becomes vital. For example, absolute values of the local CH* emissions are important to evaluate local air/fuel ratios (Lauer and Sattelmayer 2010). However, in our study, we rely on relative changes in the variance of fluctuations, which are independent of the absolute values of the measurements, but depend rather on the change in the strength of fluctuations of heat release rate. A similar approach has been utilized in recent years to investigate the dynamics of the flame near the transition (Balusamy *et al* 2015, Kheirkhah *et al* 2017, Jegal *et al* 2019, Tao and Zhou 2021).

Figure E1. The surface plot shows the slope of the increase in σ^2. The diagonal black lines show that at these regions, the increase in σ^2 is significant (99.9%) utilizing the student t-test.

Appendix C. Pearson correlation coefficients of local heat release rate fluctuations at Z1, Z2 and Z3.

We compute the correlation coefficients $CC_{\dot{q}'}$ of $\dot{q}'(t)$ between various zones. We calculate the Pearson correlation coefficient for every window as

$$CC_{\dot{q}'} = \frac{1}{N-1} \sum_{i=1}^{N} \left(\frac{\dot{a}_i'}{\sigma_{\dot{a}'}} \right) \left(\frac{\dot{b}_i'}{\sigma_{\dot{b}'}} \right), \tag{C.1}$$

where $\dot{a}'$ and $\dot{b}'$ are the time series of $\dot{q}'$ at different zones (for example Z1 and Z2), σ is the standard deviation of the respective time series. Here we used a window size (N) of 4 s to compute $CC_{\dot{q}'}$. The fluctuation $\dot{q}'(t)$ is calculated by subtracting the instantaneous quantity from a moving average of 0.04 s.

Appendix D. Spatial correlation of local heat release rate fluctuations

We calculate the spatial correlation utilizing Moran's correlation (Moran 1950) given by

$$R_{\dot{q}'} = \frac{K}{\sum_{i=1}^{l}\sum_{j=1}^{m} w_{ij}} \frac{\sum_{i=1}^{l}\sum_{j=1}^{m} w_{ij}(X_i - \overline{X})\ (X_j - \overline{X})}{\sum_{i=1}^{l}(X_i - \overline{X})^2}, \tag{D.1}$$
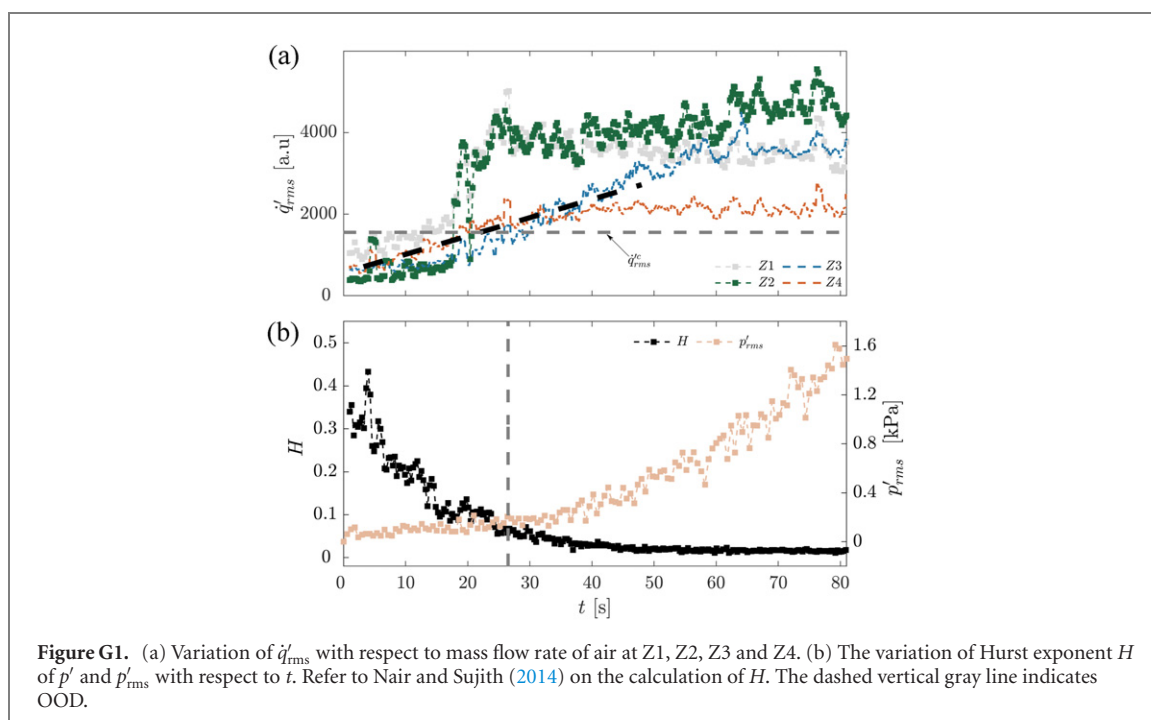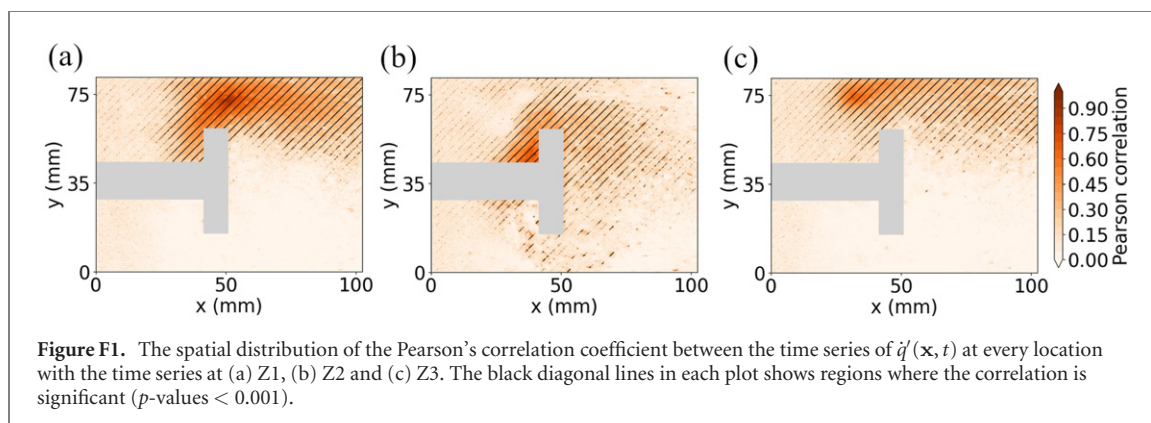
where X is the value of $\dot{q}'(\mathbf{x}, t)$ at different spatial locations indexed by l and m. K is given by $K = l \times m$. $\overline{X}$ is the spatial average of X and w_{ij} is a component of a matrix of spatial weights. Here, we have considered w_{ij} as 1.

Appendix E. Statistical significance for the increase in σ^2 of σ^2

The increase in σ^2 is estimated by the slope of the line in the time interval between 21 s and 25.5 s (figure E1). We examine this period of time because of the highest growth in σ^2 at Z1 and Z2 between 21 s and 25.5 s. In this time interval, we consider that σ^2 increases linearly. The flame zone shows a high value of the slope at Z1 and Z2 and in particular, at these regions, the increase in σ^2 is significant (99.9%) utilizing the student t-test. In the wake, the significance is weaker, indicated by grainy diagonal lines.

Appendix F. Statistical significance for the Pearson correlation

The surface plot in figures F1(a)–(c) shows the Pearson's correlation coefficient between the time series of $\dot{q}'(\mathbf{x}, t)$ at every location with the time series at Z1, Z2 and Z3 respectively. For example, in figure F1(a), we find that the correlation is significant around Z1, extending till Z2 and downstream of Z1. On the other hand, the correlation with Z1 is not significant for areas downstream of the shaft and upstream of the bluff body. The correlation is calculated for the time interval between 10 s to 20 s, which is the same time period used to check the significance of the increase in correlation in figure 5(a).

Figure F1. The spatial distribution of the Pearson's correlation coefficient between the time series of $\dot{q}'(\mathbf{x}, t)$ at every location with the time series at (a) Z1, (b) Z2 and (c) Z3. The black diagonal lines in each plot shows regions where the correlation is significant (p-values < 0.001).

Figure G1. (a) Variation of $\dot{q}'_{rms}$ with respect to mass flow rate of air at Z1, Z2, Z3 and Z4. (b) The variation of Hurst exponent H of p' and p'_{rms} with respect to t. Refer to Nair and Sujith (2014) on the calculation of H. The dashed vertical gray line indicates OOD.

Appendix G. Relation of the critical value of p' with the Hurst exponent of p'

Figure G1(a) is similar to figure 6 but with the addition of $\dot{q}'_{rms}$ at Z4. Figure G1(b) indicates that the Hurst exponent H decreases and becomes nearly constant after $t = 41$ ($\dot{m}_{air} = 660$ SLPM). At the intersection point of Z2 and Z4, we find H as 0.1.

ORCID iDs

N B George https://orcid.org/0000-0003-4123-6944

References

Akkerman V y and Law C K 2013 Effect of acoustic coupling on power-law flame acceleration in spherical confinement *Phys. Fluids* **25** 013602

Ball P and Borley N R 1999 *The Self-Made Tapestry: Pattern Formation in Nature* (Oxford: Oxford University Press)

Balusamy S, Li L K B, Han Z, Juniper M P and Hochgreb S 2015 Nonlinear dynamics of a self-excited thermoacoustic system subjected to acoustic forcing *Proc. Combust. Inst.* **35** 3229–36

Bayliss A and Matkowsky B J 1991 Bifurcation, pattern formation and chaos in combustion *Dynamical Issues in Combustion Theory* (New York, NY: Springer) pp 1–35

Biggs R 2009 Rocketdyne-F-1 Saturn V first stage engine *Remembering the Giants: Apollo Rocket Propulsion Development* (Washington, DC: National Aeronautics and Space Administration, NASA History Division, Office of External Relations) pp 15–26

Blomshield F S, Mathes H B, Crump J E, Beiter C A and Beckstead M W 1997 Nonlinear stability testing of full-scale tactical motors *J. Propul. Power* **13** 356–66

Bonciolini G and Noiray N 2019 Bifurcation dodge: avoidance of a thermoacoustic instability under transient operation *Nonlinear Dyn.* **96** 703–16

Brown G L and Roshko A 1974 On density effects and large structure in turbulent mixing layers *J. Fluid Mech.* **64** 775–816

Busse F H 1978 Non-linear properties of thermal convection *Rep. Prog. Phys.* **41** 1929–67

Candel S M 1992 Combustion instabilities coupled by pressure waves and their active control *Symp. (Int.) on Combustion* vol 24 (Elsevier) pp 1277–96

Cantwell B J 1981 Organized motion in turbulent flow *Annu. Rev. Fluid Mech.* **13** 457–515

Chang W, Stein M L, Wang J, Kotamarthi V R and Moyer E J 2016 Changes in spatiotemporal precipitation patterns in changing climate conditions *J. Climate* **29** 8355–76

Chen G, Li Z, Tang L and Yu Z 2021 Mutual synchronization of self-excited acoustic oscillations in coupled thermoacoustic oscillators *J. Phys.* D **54** 485504

Croquette V 1989 Convective pattern dynamics at low Prandtl number: part I *Contemp. Phys.* **30** 113–33

Cross M C and Hohenberg P C 1993 Pattern formation outside of equilibrium *Rev. Mod. Phys.* **65** 851–1112

Delage R, Takayama Y and Biwa T 2017 On–off intermittency in coupled chaotic thermoacoustic oscillations *Chaos* **27** 043111

Ducruix S, Schuller T, Durox D and Candel S 2003 Combustion dynamics and instabilities: elementary coupling and driving mechanisms *J. Propul. Power* **19** 722–34

Frenkel D 2006 Seeds of phase change *Nature* **443** 641

George N B, Unni V R, Raghunathan M and Sujith R I 2018 Pattern formation during transition from combustion noise to thermoacoustic instability via intermittency *J. Fluid Mech.* **849** 615–44

Godavarthi V, Kasthuri P, Mondal S, Sujith R I, Marwan N and Kurths J 2020 Synchronization transition from chaos to limit cycle oscillations when a locally coupled chaotic oscillator grid is coupled globally to another chaotic oscillator *Chaos* **30** 033121

Gopalakrishnan E A, Sharma Y, John T, Dutta P S and Sujith R I 2016 Early warning signals for critical transitions in a thermoacoustic system *Sci. Rep.* **6** 1–10

Gotoda H, Nikimoto H, Miyano T and Tachibana S 2011 Dynamic properties of combustion instability in a lean premixed gas-turbine combustor *Chaos* **21** 013124

Gotoda H, Shinoda Y, Kobayashi M, Okuno Y and Tachibana S 2014 Detection and control of combustion instability based on the concept of dynamical system theory *Phys. Rev.* E **89** 022910

Hachijo T, Masuda S, Kurosaka T and Gotoda H 2019 Early detection of thermoacoustic combustion oscillations using a methodology combining statistical complexity and machine learning *Chaos* **29** 103123

Hong S, Speth R L, Shanbhogue S J and Ghoniem A F 2013 Examining flow-flame interaction and the characteristic stretch rate in vortex-driven combustion dynamics using PIV and numerical simulation *Combust. Flame* **160** 1381–97

Jegal H, Moon K, Gu J, Li L K B and Kim K T 2019 Mutual synchronization of two lean-premixed gas turbine combustors: phase locking and amplitude death *Combust. Flame* **206** 424–37

Juniper M P and Sujith R I 2018 Sensitivity and nonlinearity of thermoacoustic oscillations *Annu. Rev. Fluid Mech.* **50** 661–89

Kanders K, Lee H, Hong N, Nam Y and Stoop R 2020 Fingerprints of a second order critical line in developing neural networks *Commun. Phys.* **3** 1–13

Kheirkhah S, Geraedts B D, Saini P, Venkatesan K and Steinberg A M 2017 Non-stationary local thermoacoustic phase relationships in a gas turbine combustor *Proc. Combust. Inst.* **36** 3873–80

Kline S J, Reynolds W C, Schraub F A and Runstadler P W 1967 The structure of turbulent boundary layers *J. Fluid Mech.* **30** 741–73

Kobayashi T, Murayama S, Hachijo T and Gotoda H 2019 Early detection of thermoacoustic combustion instability using a methodology combining complex networks and machine learning *Phys. Rev. Appl.* **11** 064034

Komarek T and Polifke W 2010 Impact of swirl fluctuations on the flame response of a perfectly premixed swirl burner *J. Eng. Gas Turbine. Power* **132** 061503

Lauer M and Sattelmayer T 2010 On the adequacy of chemiluminescence as a measure for heat release in turbulent flames with mixture gradients *J. Eng. Gas Turbine. Power* **132** 061502

Lee Rodgers J and Nicewander W A 1988 Thirteen ways to look at the correlation coefficient *Am. Stat.* **42** 59–66

Lieuwen T C 2002 Experimental investigation of limit-cycle oscillations in an unstable gas turbine combustor *J. Propul. Power* **18** 61–7

Lieuwen T C 2012 *Unsteady Combustor Physics* (Cambridge: Cambridge University Press)

Lieuwen T C and Yang V 2005 *Combustion Instabilities in Gas Turbine Engines: Operational Experience, Fundamental Mechanisms, and Modeling* (Reston, Virginia: American Institute of Aeronautics and Astronautics)

Ludescher J *et al* 2021 Network-based forecasting of climate phenomena *Proc. Natl Acad. Sci.* **118**

Madjarova V D, Kadono H and Toyooka S 2003 Dynamic electronic speckle pattern interferometry (DESPI) phase analyses with temporal Hilbert transform *Opt. Express* **11** 617–23

McManus K R, Poinsot T and Candel S M 1993 A review of active control of combustion instabilities *Prog. Energy Combust. Sci.* **19** 1–29

Meron E 2016 Pattern formation—a missing link in the study of ecosystem response to environmental changes *Math. Biosci.* **271** 1–18

Moon K, Guan Y, Li L K and Kim K T 2020 Mutual synchronization of two flame-driven thermoacoustic oscillators: dissipative and time-delayed coupling effects *Chaos* **30** 023110

Mondal S, Unni V R and Sujith R I 2017 Onset of thermoacoustic instability in turbulent combustors: an emergence of synchronized periodicity through formation of chimera-like states *J. Fluid Mech.* **811** 659–81

Moran P A P 1950 Notes on continuous stochastic phenomena *Biometrika* **37** 17–23

Nair V and Sujith R I 2014 Multifractality in combustion noise: predicting an impending combustion instability *J. Fluid Mech.* **747** 635–55

Nair V, Thampi G, Karuppusamy S, Gopalan S and Sujith R I 2013 Loss of chaos in combustion noise as a precursor of impending combustion instability *Int. J. Spray Combust. Dyn.* **5** 273–90

Nair V, Thampi G and Sujith R I 2014 Intermittency route to thermoacoustic instability in turbulent combustors *J. Fluid Mech.* **756** 470–87

Pavithran I and Sujith R I 2021 Effect of rate of change of parameter on early warning signals for critical transitions *Chaos* **31** 013116

Pawar S A, Seshadri A, Unni V R and Sujith R I 2017 Thermoacoustic instability as mutual synchronization between the acoustic field of the confinement and turbulent reactive flow *J. Fluid Mech.* **827** 664–93

Poinsot T J, Trouve A C, Veynante D P, Candel S M and Esposito E J 1987 Vortex-driven acoustically coupled combustion instabilities *J. Fluid Mech.* **177** 265–92

Premchand C P, George N B, Raghunathan M, Unni V R, Sujith R I and Nair V 2019 Lagrangian analysis of intermittent sound sources in the flow-field of a bluff-body stabilized combustor *Phys. Fluids* **31** 025115

Raghunathan M, George N B, Unni V R, Midhun P R, Reeja K V and Sujith R I 2020 Multifractal analysis of flame dynamics during transition to thermoacoustic instability in a turbulent combustor *J. Fluid Mech.* **888**

Rastogi B, Williams A P, Fischer D T, Iacobellis S F, McEachern K, Carvalho L, Jones C, Baguskas S A and Still C J 2016 Spatial and temporal patterns of cloud cover and fog inundation in coastal California: ecological implications *Earth Interact.* **20** 1–19

Rayleigh J W S 1878 The explanation of certain acoustical phenomena *Nature* **18** 319–21

Rocha J C, Peterson G, Bodin Ö and Levin S 2018 Cascading regime shifts within and across scales *Science* **362** 1379–83

Schadow K, Gutmark E, Parr T, Parr D, Wilson K and Crump J 1989 Large-scale coherent structures as drivers of combustion instability *Combust. Sci. Technol.* **64** 167–86

Scheffer M, Carpenter S, Foley J A, Folke C and Walker B 2001 Catastrophic shifts in ecosystems *Nature* **413** 591–6

Sengupta U, Rasmussen C E and Juniper M P 2020 Bayesian machine learning for the prognosis of combustion instabilities from noise *ASME Turbo Expo 2020: Turbomachinery Technical Conf. and Exposition* (American Society of Mechanical Engineers Digital Collection)

Silva C F, Merk M, Komarek T and Polifke W 2017 The contribution of intrinsic thermoacoustic feedback to combustion noise and resonances of a confined turbulent premixed flame *Combust. Flame* **182** 269–78

Stolbova V, Surovyatkina E, Bookhagen B and Kurths J 2016 Tipping elements of the Indian monsoon: prediction of onset and withdrawal *Geophys. Res. Lett.* **43** 3982–90

Sujith R I and Unni V R 2020a Complex system approach to investigate and mitigate thermoacoustic instability in turbulent combustors *Phys. Fluids* **32** 061401

Sujith R I and Unni V R 2020b Dynamical systems and complex systems theory to study unsteady combustion *Proc. Comb. Inst.* **38** 3445

Surovyatkina E D 2004 Rise and saturation of the correlation time near bifurcation threshold *Phys. Lett.* A **329** 169–72

Surovyatkina E, Kravtsov Y A and Kurths J 2005 Fluctuation growth and saturation in nonlinear oscillators on the threshold of bifurcation of spontaneous symmetry breaking *Phys. Rev.* E **72** 046125

Sutton G P 2003 History of liquid-propellant rocket engines in Russia, formerly the Soviet Union *J. Propul. Power* **19** 1008–37

Tao C and Zhou H 2021 Effects of operating parameters on the combustion oscillation behaviour in a lean premixed CH_4 combustor *J. Mech. Sci. Technol.* **35** 3753–62

Tony J, Gopalakrishnan E, Sreelekha E and Sujith R 2015 Detecting deterministic nature of pressure measurements from a turbulent combustor *Phys. Rev.* E **92** 062902

Unni V R, Krishnan A, Manikandan R, George N B, Sujith R I, Marwan N and Kurths J 2018 On the emergence of critical regions at the onset of thermoacoustic instability in a turbulent combustor *Chaos* **28** 063125

Unni V R, Mukhopadhyay A and Sujith R I 2015 Online detection of impending instability in a combustion system using tools from symbolic time series analysis *Int. J. Spray Combust. Dyn.* **7** 243–55

Yang H, Shew W L, Roy R and Plenz D 2012 Maximal variability of phase synchrony in cortical networks with neuronal avalanches *J. Neurosci.* **32** 1061–72

Yu K H, Trouvé A and Daily J W 1991 Low-frequency pressure oscillations in a model ramjet combustor *J. Fluid Mech.* **232** 47–72